Check for updates

OPEN

Origin of enhanced chemical precompression in cerium hydride CeH$_9$

Hyunsoo Jeon, Chongze Wang, Seho Yi & Jun-Hyung Cho✉

The rare-earth metal hydrides with clathrate structures have been highly attractive because of their promising high-T_c superconductivity at high pressure. Recently, cerium hydride CeH$_9$ composed of Ce-encapsulated clathrate H cages was synthesized at much lower pressures of 80–100 GPa, compared to other experimentally synthesized rare-earth hydrides such as LaH$_{10}$ and YH$_6$. Based on density-functional theory calculations, we find that the Ce $5p$ semicore and $4f/5d$ valence states strongly hybridize with the H $1s$ state, while a transfer of electrons occurs from Ce to H atoms. Further, we reveal that the delocalized nature of Ce $4f$ electrons plays an important role in the chemical precompression of clathrate H cages. Our findings not only suggest that the bonding nature between the Ce atoms and H cages is characterized as a mixture of ionic and covalent, but also have important implications for understanding the origin of enhanced chemical precompression that results in the lower pressures required for the synthesis of CeH$_9$.

In recent years, rare-earth metal hydrides have attracted much attention due to the possibility of their realization of room-temperature superconductivity (SC)[1–8]. First-principles density-functional theory (DFT) calculations together with the Migdal–Eliashberg formalism have predicted that rare-earth metal hydrides such as yttrium, lanthanum, cerium hydrides host high-T_c SC at megabar pressures[9,10], the origin of which is based on phonon-mediated electron pairing[11]. Subsequently, such a conventional SC of LaH$_{10}$ was experimentally observed with a superconducting transition temperature T_c of 250–260 K at a pressure of ∼170 GPa[3,4]. This T_c record of LaH$_{10}$ has been the highest temperature so far among experimentally available superconducting materials including cuprates[12,13] and Fe-based superconductors[14,15]. Therefore, the experimental realization of room-temperature SC in LaH$_{10}$ has stimulated interests of the high-T_c community towards compressed metal hydrides under high pressure[16–23].

However, since the synthesis of LaH$_{10}$ was performed at ∼170 GPa[3,4], it has been quite demanding to discover H-rich rare-earth hydrides synthesized at a moderate pressure below ∼100 GPa, which is easily and routinely achievable in the diamond anvil cell (DAC)[24,25]. Motivated by the first theoretical prediction[9] of cerium hydride CeH$_9$ with a clathrate hydrogen cage structure, two experimental groups[5,6] achieved its successful synthesis at a lower pressure of 80–100 GPa. X-ray diffraction measurements and DFT calculations[5,6] confirmed the previously predicted[9] crystal structure of CeH$_9$, which adopts a hexagonal clathrate structure with the space group P6$_3$/mmc. Here, each Ce atom is surrounded by the H$_{29}$ cage consisting of 29 H atoms (see Fig. 1a). It is remarkable that the H–H bond lengths in CeH$_9$ are close to those of solid metallic hydrogen that can be produced at high pressure above 400 GPa[26–29]. Therefore, the discovery of CeH$_9$ having clathrate hydrogen networks suggests that the metallic state of solid hydrogen can be attained at relatively lower pressures by using binary hydrides with f-electron metals. It is noteworthy that the sizable reduction of H–H bond lengths in CeH$_9$ reflects the presence of a larger chemical precompression[30–32] compared to other rare-earth metal hydrides such as LaH$_{10}$ and YH$_{10}$[9,10,33–37]. However, the underlying mechanism of how the pressure required for the synthesis of CeH$_9$ is much reduced is yet to be identified.

In this paper, we investigate the electronic structure and bonding properties of CeH$_9$ at high pressure using first-principles DFT calculations with the inclusion of Hubbard on-site Coulomb interaction. The calculated band structure of CeH$_9$ shows a strong hybridization of the Ce $5p$ semicore and $4f/5d$ valence states with the H $1s$ state. We reveal that the delocalized nature of Ce $4f$ electrons contributes to yield a much larger chemical

Department of Physics, Research Institute for Natural Science, and Institute for High Pressure at Hanyang University, Hanyang University, 222 Wangsimni-ro, Seongdong-ku, Seoul 04763, Republic of Korea. ✉email: chojh@hanyang.ac.kr
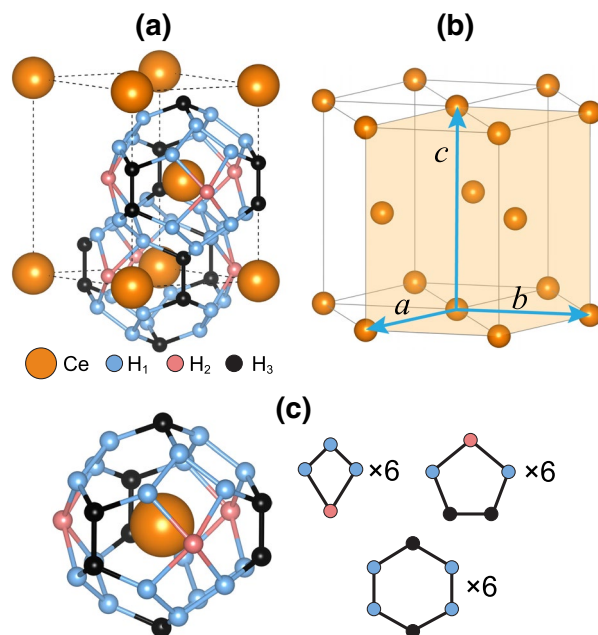
Figure 1. (a) Optimized structure of CeH_9 at 100 GPa and (b) hexagonal-close-packed (hcp) lattice of Ce atoms. Three different species of H atoms, H_1, H_2, and H_3, exist in H_{29} cage. The isolated H_{29} cage surrounding a Ce atom is displayed in (c), together with its constituent parts, i.e., six tetragon rings, six pentagon rings, and six hexagon rings.

precompression of clathrate H_{29} cages along the c axis than in the a–b plane. Despite a strong hybridization between the Ce- and H-derived electronic states, our Bader charge analysis shows a charge transfer from Ce to H atoms, thereby suggesting that the bonding nature between the Ce atoms and H_{29} cages features the mixed ionic and covalent bonding. The present results provide new insight into understanding the underlying mechanism of the chemical precompression that requires relatively lower pressures for the synthesis of CeH9[5,6], compared to other experimentally synthesized rare-earth hydrides LaH10[3,4] and YH6[7,8].

Results and discussion

We begin by optimizing the structure of CeH_9 using the PBE + U calculation. Figure 1a shows the optimized structure of CeH_9 at a pressure of 100 GPa, which is the same pressure employed in previous DAC experiments[5,6]. Here, Ce atoms form a hcp lattice (see Fig. 1b) with the lattice constants $a = b = 3.717$ Å and $c = 5.666$ Å, in good agreement with the experimental[5,6] data of $a = b = 3.66$ Å and $c = 5.58$ Å. Meanwhile, the H_{29} cage surrounding a Ce atom is constituted by six tetragon rings, six pentagon rings, and six hexagon rings (see Fig. 1c). Note that there are three species of H atoms [termed H_1, H_2, and H_3 in Fig. 1a composing the H_{29} cage. We find that the $H_1 - H_1$, $H_1 - H_2$, $H_1 - H_3$, and $H_3 - H_3$ bond lengths are 1.190, 1.486, 1.275, and 1.065 Å, respectively. These H–H bond lengths in CeH_9 are close to those (0.98 and 1.21 Å) predicted from metallic hydrogen at ~500 GPa[28]. It is thus likely that the synthesized[5,6] binary compound CeH_9 with the clathrate H_{29} cages is able to generate H networks comparable to metallic hydrogen even at a low pressure of 100 GPa.

Figure 2a shows the calculated total charge density ρ_{tot} of CeH_9. It is seen that H atoms in the H_{29} cage are bonded to each other with covalent-like bonding. Here, the charge densities of H–H and Ce–H bonds exhibit the saddle-point characters at their midpoints, similar to that of the C–C covalent bond in diamond[38]. As shown in Fig. S1 in the Supplementary information, the calculated electron localization function also shows the covalent-like H–H and Ce–H bonds. The charge densities at the midpoints of the $H_1 - H_2$, $H_1 - H_3$, and $H_3 - H_3$ bonds are 0.39, 0.56, and 0.85 $e/Å^3$, respectively. These values in CeH_9 are larger than the corresponding ones (0.32, 0.45, and 0.76 $e/Å^3$ in Fig. 2b) obtained from the isolated H_{29} cages whose structure is taken from the optimized structure of CeH_9. This result implies that the H–H covalent bonds in CeH_9 are strengthened by a charge transfer from Ce to H atoms. Interestingly, the electrical charges of Ce and H atoms are connected to each other, reflecting a covalent-like bonding character. It is noteworthy that the charge densities at the points marked "×" (in Fig. 2a) between Ce and H_1/H_2/H_3 atoms are close to that at the midpoint of the $H_1 - H_2$ bond. This covalent nature of Ce–H bonds is attributed to a strong hybridization between the Ce and H electronic states, as discussed below.

To examine the charge transfer between Ce to H atoms, we calculate the charge density difference, defined as $\Delta\rho = \rho_{tot} - \rho_{Ce} - \rho_H$, where ρ_{Ce} and ρ_H represent the charge densities of the isolated Ce lattice (Fig. 1b) and the isolated H_{29} cages (Fig. 2b), respectively. As shown in Fig. 2c, $\Delta\rho$ illustrates how electronic charge is transferred from Ce to H atoms. It is seen that the charge transfer occurs mostly from Ce to H_1 and H_2. Meanwhile, the charge transfer from Ce to H_3 is minor. We further calculate the Bader charges[39] of CeH_9 to estimate the number of transferred electrons between Ce and H atoms. Figure 2d shows the Bader basins of the constituent atoms, obtained from the gradient of ρ_{tot}[39]. We find that the calculated Bader charges of Ce, H_1, H_2, and H_3 basins are
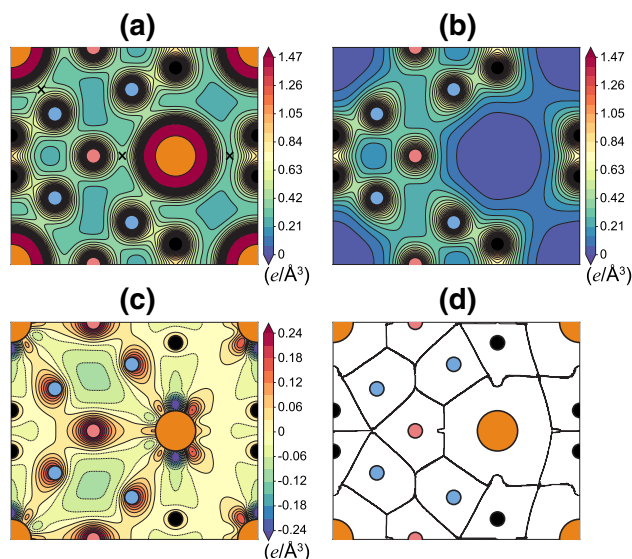
Figure 2. Calculated total charge density ρ_{tot} of (**a**) CeH$_9$ and (**b**) isolated H$_{29}$ cages. The saddle points of charge densities between Ce and H$_1$/H$_2$/H$_3$ atoms are marked "×" in (**a**). The charge densities in (**a**) and (**b**) are plotted on the (110) plane with the contour spacings of 0.07 e/Å^3. The charge density difference $\Delta\rho$ (defined in the text) is displayed in (**c**), with the contour spacing of ±0.03 e/Å^3. The Bader basins of Ce and H atoms are displayed in (**d**).
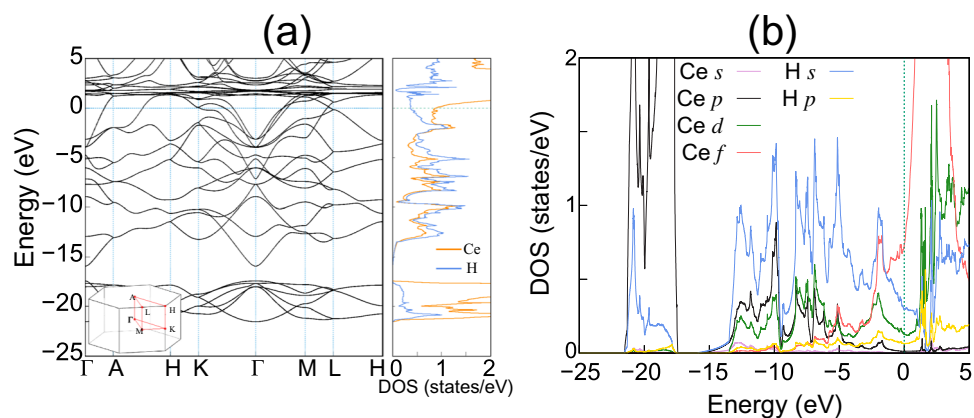

Figure 3. (**a**) Calculated band structure of CeH$_9$ together with the LDOS for Ce and H atoms. The energy zero represents E_F. The PDOS of CeH$_9$ is also given in (**b**).

$-9.47e$ (including the $5s^2 5p^6$ semicore electrons), $-1.34e$, $-1.31e$, and $-1.09e$, respectively. Thus, we can say that Ce atoms lose electrons of 2.53e per atom, while H$_1$, H$_2$, and H$_3$ atoms gain electrons of 0.34e, 0.31e, 0.09e per atom, respectively.

In Fig. 3a, we display the calculated band structure of CeH$_9$, together with the local density of states (LDOS) for Ce and H atoms. The narrow bands located at $\sim$2 eV above E_F originate from Ce 4f electrons, while those located at around -20 eV below E_F are associated with Ce 5p semicore electrons. It is noticeable that the LDOS shape of Ce atoms is very similar to that of H atoms in the energy range between -15 eV and E_F, indicating a strong hybridization between Ce and H electronic states. In order to resolve the orbital characters of electronic states, we plot the partial density of states (PDOS) projected onto the Ce 5p-semicore and 4f/5d-valence states and the H 1s state in Fig. 3b. We find that the Ce 5p-semicore states are extended upward to reach up to E_F, while the 4f- and 5d-valence states are distributed downward to about -10 and -13 eV below E_F, respectively. Hence, these delocalized semicore and valence states hybridize well with the H 1s state. Such a strong hybridization between Ce and H electrons is likely associated with the Ce-encapsulated spherical H-cage structure of CeH$_9$. Consequently, the electron charges of Ce and H atoms show covalent characteristics between the Ce and H$_1$/H$_2$/H$_3$ atoms (see the "×" points in Fig. 2a). Based on this covalent feature of the Ce–H bonds and the charge transfer from Ce to H atoms, we can say that the bonding nature between the Ce atoms to H$_{29}$ cages is characterized as a mixture of ionic and covalent.
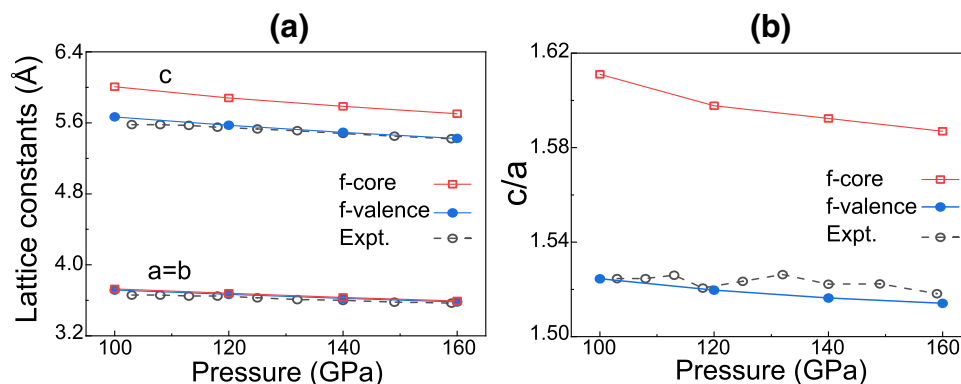
Figure 4. (**a**) Calculated lattice constants of CeH_9 as a function of pressure using the f-valence scheme, in comparison with those obtained using the f-core scheme and experiment[5]. The resulting c/a ratios as a function of pressure are also given in (**b**).

As mentioned above, the synthesis of CeH_9 requires much lower pressures 80–100 GPa[5,6] compared to that (~170 GPa) for the synthesis of LaH_{10}[3,4], indicating the variation of chemical precompression with respect to the occupation of f electrons. Here, we note that Ce atom with the electron configuration $[Xe]4f^15d^16s^2$ has one $4f$ electron, while La atom with $[Xe]5d^16s^2$ represents no occupation of f orbitals. It is thus expected that the lower synthesis pressure of CeH_9 would be caused by the presence of the delocalized Ce $4f$ states (see Fig. 3b). To confirm how the delocalized nature of Ce $4f$ electrons contributes to the chemical precompression of H_{29} cages, we optimize the structure of CeH_9 as a function of pressure using the f-core scheme, where Ce $4f$ electrons are considered as core electrons. Therefore, the interactions of $4f$ electrons with valence electrons are completely removed to simulate the localized nature of $4f$ electrons[40]. The band structure and PDOS of CeH_9 calculated using the f-core scheme are displayed in Fig. S2. We find that the band dispersions of the Ce $5d$ and H $1s$ states change largely around E_F because their hybridizations with the Ce $4f$ states are avoided in the f-core scheme. In Fig. 4a, the lattice parameters computed using the f-core scheme are compared with those of the f-valence scheme as well as the experimental data[5]. We find that in the pressure range between 100 and 160 GPa, both the f-core and f-valence schemes predict similar values for a and b, close to the experimental values[5]. However, the f-core scheme predicts larger c values than the f-valence scheme and experiment[5] by ~6% in the same pressure range. As a result, in contrast to both the f-valence scheme and experiment[5], the f-core scheme gives relatively larger values of the c/a ratio between 100 and 160 GPa (see Fig. 4b). These results indicate that the delocalized nature of Ce $4f$ electrons plays an important role in determining the chemical precompression along the c axis, while it hardly affects the chemical precompression in the a–b plane.

In order to check whether the localized/delocalized nature of Ce $4f$ electrons influences the dynamical stability of CeH_9, we calculate the phonon spectrum at 100 GPa using both the f-core and f-valence schemes. The calculated phonon spectrum of the f-core scheme exhibits imaginary frequencies in the whole Brillouin zone [see Fig. S3(a) in the Supplementary information], indicating that CeH_9 is dynamically unstable. On the other hand, the f-valence scheme shows that CeH_9 is dynamically stable without any imaginary-frequency phonon mode [see Fig. S3(b)]. Therefore, we can say that the delocalized nature of Ce $4f$ electrons is necessary for stabilizing the clathrate structure of CeH_9.

Conclusion

Our first-principles DFT + U calculations for CeH_9 have shown that (i) the Ce $5p$ semicore and $4f/5d$ valence states strongly hybridize with the H $1s$ state, (ii) the charge transfer occurs mostly from Ce to H_1 and H_2 atoms, and (iii) the delocalized nature of Ce $4f$ electrons is an essential ingredient in the chemical precompression of clathrate H_{29} cages. The present results not only suggest that the bonding nature between the Ce atoms and H cages is characterized as a mixture of ionic and covalent, but also provide an explanation for the enhanced chemical precompression in CeH_9. We thus proposed that the large chemical precompression of H-rich clathrate structures can be attained in rare-earth hydrides with delocalized $4f$ electrons. It is noteworthy that, according to DFT calculations, PrH_9[16] with clathrate H cages begins to destabilize at a pressure below about ~100 GPa, which is relatively lower than that (226 GPa) of YH_{10}[36]. These different destabilization pressures of PrH_9 and YH_{10} are likely to reflect the variation of chemical precompression, due to the influence of delocalized f electrons. Indeed, PrH_9 was experimentally synthesized at a pressure of ~100 GPa[16]. We also note that YH_6 containing no f electrons begins to destabilize at a pressure below ~72 GPa, which is much lower than that (~226 GPa) of YH_{10}[36]. Here, the different stabilization pressures of YH_6 and YH_{10} were explained[36] in terms of the size of Y atom: i.e., YH_{10} having denser, larger hydrogen cages with shorter H–H distances requires a higher stabilization pressure.

Methods

Our DFT calculations were performed using the Vienna ab initio simulation package with the projector-augmented wave method[41–43]. For the exchange-correlation energy, we employed the generalized-gradient approximation functional of Perdew–Burke–Ernzerhof (PBE)[44]. The $5s^25p^6$ semicore electrons of Ce atom were included

4

in the electronic-structure calculations. For Ce $4f$ electrons, we considered the effective on-site Coulomb interaction of $U_{eff}(=U-J) = 4$ eV, where the Hubbard parameter U is 4.5 eV and the exchange interaction parameter J is 0.5 eV[5]. A plane-wave basis was used with a kinetic energy cutoff of 1000 eV. The **k**-space integration was done with $12 \times 12 \times 8$ k points for the structure optimization and $24 \times 24 \times 16$ k points for the DOS calculation. All atoms were allowed to relax along the calculated forces until all the residual force components were less than 0.005 eV/Å. Phonon calculations were preformed by a finite displacement method with the PHONOPY code[45].

References

1. Bi, T., Zarifi, N., Terpstra, T. & Zurek, E. *The Search for Superconductivity in High Pressure Hydrides* (Reference Module in Chemistry, Molecular Science and Chemical Engineering, 2020).
2. Flores-Livas, J. A. *et al.* A perspective on conventional high-temperature superconductors at high pressure: Methods and materials. *Phys. Rep.* **856**, 1 (2020).
3. Somayazulu, M. *et al.* Evidence for superconductivity above 260 K in lanthanum superhydride at megabar pressures. *Phys. Rev. Lett.* **122**, 027001 (2019).
4. Drozdov, A. P. *et al.* Superconductivity at 250 K in lanthanum hydride under high pressures. *Nature* **569**, 528 (2019).
5. Li, X. *et al.* Polyhydride CeH₉ with an atomic-like hydrogen clathrate structure. *Nat. Commun.* **10**, 3461 (2019).
6. Salke, N. P. *et al.* Synthesis of clathrate cerium superhydride CeH₉ at 80–100 GPa with atomic hydrogen sublattice. *Nat. Commun.* **10**, 4453 (2019).
7. Kong, P. P. *et al.* Superconductivity up to 243 K in yttrium hydrides under high pressure. arXiv:1909.10482 (2019).
8. Troyan, I. A. *et al.* Synthesis and superconductivity of yttrium hexahydride Im3̄m-YH₆. arXiv:1908.01534 (2019).
9. Peng, F. *et al.* Hydrogen clathrate structures in rare earth hydrides at high pressures: Possible route to room-temperature superconductivity. *Phys. Rev. Lett.* **119**, 107001 (2017).
10. Liu, H., Naumov, I. I., Hoffmann, R., Ashcroft, N. W. & Hemley, R. J. Potential high-Tc superconducting lanthanum and yttrium hydrides at high pressure. *Proc. Natl. Acad. Sci. USA* **114**, 6990 (2017).
11. Bardeen, J., Cooper, L. N. & Schrieffer, J. R. Microscopic theory of superconductivity. *Phys. Rev.* **106**, 162 (1957).
12. Schilling, A., Cantoni, M., Guo, J. D. & Ott, H. R. Superconductivity above 130 K in the Hg-Ba-Ca-Cu-O system. *Nature* **363**, 56 (1993).
13. Varma, C. High-temperature superconductivity: Mind the pseudogap. *Nature* **468**, 184 (2010).
14. Yang, J. *et al.* Superconductivity at 53.5 K in GdFeAsO₁₋δ. *Supercond. Sci. Technol.* **21**, 8 (2008).
15. Wu, G. *et al.* Superconductivity at 56 K in samarium-doped SrFeAsF. *J. Phys. Condens. Matter* **21**, 14 (2009).
16. Zhou, D. *et al.* Superconducting praseodymium superhydrides.. *Sci. Adv.* **6**, eaax6849 (2020).
17. Zhou, D. *et al.* High-pressure synthesis of magnetic neodymium polyhydrides. *J. Am. Chem. Soc.* **142**, 2803 (2020).
18. Salke, N. P. *et al.* Prediction and synthesis of dysprosium hydride phases at high pressure. *Inorg. Chem.* **59**, 5303 (2020).
19. Mozaffari, S. *et al.* Superconducting phase diagram of H₃S under high magnetic fields. *Nat. Commun.* **10**, 2522 (2019).
20. Lesik, M. *et al.* Magnetic measurements on micrometer-sized samples under high pressure using designed NV centers. *Science* **366**, 1359 (2019).
21. Sun, Y., Lv, J., Xie, Y., Liu, H. & Ma, Y. Route to a superconducting phase above room temperature in electron-doped hydride compounds under high pressure. *Phys. Rev. Lett.* **123**, 097001 (2019).
22. Zhao, Z. *et al.* Predicted pressure-induced superconducting transition in electride Li₆P. *Phys. Rev. Lett.* **122**, 097002 (2019).
23. Ma, L. *et al.* Experimental syntheses of sodalite-like clathrate EuH₆ and EuH₉ at extreme pressure. arXiv:2002.09900 (2020).
24. Bassett, W. A. Diamond anvil cell 50th birthday. *High Press. Res.* **29**, 163 (2009).
25. Mao, H. K., Chen, X. J., Ding, Y., Li, B. & Wang, L. Solids, liquids, and gases under high pressure. *Rev. Mod. Phys.* **90**, 015007 (2018).
26. McMahon, J. M., Morales, M. A., Pierleoni, C. & Ceperley, D. M. The properties of hydrogen and helium under extreme conditions. *Rev. Mod. Phys.* **84**, 1607 (2012).
27. McMinis, J., Clay, R. C., Lee, D. & Morales, M. A. Molecular to atomic phase transition in hydrogen under high pressure. *Phys. Rev. Lett.* **114**, 105305 (2015).
28. Borinaga, M., Errea, I., Calandra, M., Mauri, F. & Bergara, A. Anharmonic effects in atomic hydrogen: superconductivity and lattice dynamical stability. *Phys. Rev. B* **93**, 174308 (2016).
29. Dias, R. P. & Silvera, I. F. Observation of the Wigner-Huntington transition to metallic hydrogen. *Science* **355**, 715 (2017).
30. Ashcroft, N. W. Hydrogen dominant metallic alloys: High temperature superconductors?. *Phys. Rev. Lett.* **92**, 187002 (2004).
31. Feng, J. *et al.* Structures and potential superconductivity in SiH₄ at high pressure: En route to "metallic hydrogen". *Phys. Rev. Lett.* **96**, 017006 (2006).
32. Eremets, M. I., Trojan, I. A., Medvedev, S. A., Tse, J. S. & Yao, Y. Superconductivity in hydrogen dominant materials: Silane. *Science* **319**, 1506 (2008).
33. Liu, L. *et al.* Microscopic mechanism of room-temperature superconductivity in compressed LaH₁₀. *Phys. Rev. B* **99**, 140501(R) (2019).
34. Wang, C., Yi, S. & Cho, J.-H. Pressure depencence of the superconducting transition temperature of comprresed LaH₁₀. *Phys. Rev. B* **100**, 060502(R) (2019).
35. Wang, C., Yi, S. & Cho, J.-H. Multiband nature of room-temperature superconductivity in LaH₁₀ at high pressure. *Phys. Rev. B* **101**, 104506 (2020).
36. Heil, C., Cataldo, S., Bachelet, G. B. & Boeri, L. Superconductivity in sodalite-like yttrium hydride clarhartes. *Phys. Rev. B* **99**, 220502(R) (2019).
37. Errea, I. *et al.* Quantum crystal structure in the 250-kelvin superconducting lanthanum hydride. *Nature (London)* **578**, 66 (2020).
38. Kaxiras, E. *Atomic and Electronic Structure of Solids* 152 (Cambridge University Press, New York, 2003).
39. Bader, R. F. W. Atoms in molecules. *Acc. Chem. Res.* **18**, 9 (1985).
40. Kim, J., Kim, K., Choi, H. C. & Min, B. I. Volume contraction in CeB₄ induced by delocalized Ce $4f$ electrons. *Phys. Rev. B* **84**, 113108 (2011).
41. Kresse, G. & Hafner, J. Ab initio molecular dynamics for open-shell transition metals. *Phys. Rev. B* **48**, 13115 (1993).
42. Kresse, G. & Furthmüller, J. Efficiency of ab-initio total energy calculations for metals and semiconductors using a plane-wave basis set. *Comput. Mater. Sci.* **6**, 15 (1996).
43. Blöchl, P. E. Projector augmented-wave method. *Phys. Rev. B* **50**, 17953 (1994).
44. Perdew, J. P., Burke, K. & Ernzerhof, M. Generalized gradient approximation made simple. *Phys. Rev. Lett.* **1996**, 77, 3865; **78**, 1396 (1997).
45. Togo, A. & Tanaka, I. First principles phonon calculations in materials science. *Scr. Mater.* **108**, 1 (2015).

Author contributions

H.J., C.W., and S.Y. contributed equally to this work. J.H.C. designed the research; H.J. and C.W. performed the theoretical calculations; all the authors analyzed the data and wrote the paper.

Competing interests

The authors declare no competing interests.

Additional information

Supplementary information is available for this paper at https://doi.org/10.1038/s41598-020-73665-1.

Correspondence and requests for materials should be addressed to J.-H.C.

Reprints and permissions information is available at www.nature.com/reprints.

Publisher's note Springer Nature remains neutral with regard to jurisdictional claims in published maps and institutional affiliations.